Nanoscale

PAPER

View Article Online
View Journal | View Issue

Check for updates

Cite this: *Nanoscale*, 2019, **11**, 22359

$CsRe_2F_7$@glass nanocomposites with efficient up-/down-conversion luminescence: from *in situ* nanocrystallization synthesis to multi-functional applications†

Jiangkun Chen,[a,b,c] Shaoxiong Wang,[a,b,c] Jidong Lin[a,b,c] and Daqin Chen *[a,b,c]

Recently, lanthanide-doped luminescent materials have been widely studied and most investigations have been limited to rare-earth-containing fluorides formed with lighter alkali metals (Li, Na and K). Hence, it is important to understand the luminescence properties of cesium rare-earth fluorides. Herein, a novel type of multi-functional luminescent material, hexagonal β-$CsRe_2F_7$ (Re = La–Lu, Y, Sc) nanocrystals, is successfully prepared *via in situ* crystallization inside glass. Specifically, Yb/Er:β-$CsLu_2F_7$@glass exhibits a much higher upconversion quantum yield than Yb/Er:β-$NaYF_4$@glass (about 6 times), which is believed to be one of the most efficient upconversion materials so far. Impressively, Er:$CsYb_2F_7$@glass shows a significant photothermal effect, which can produce variable upconversion emission colors induced by an incident 980 nm laser diode, enabling it to find practical application in novel/high-precision anti-counterfeiting. In addition, Ce:$CsLu_2F_7$@glass with a maximal photoluminescence quantum yield reaching 67% can yield intense X-ray excitable radioluminescence, which is even higher than that of a commercial $Bi_4Ge_3O_{12}$ scintillator. Benefitting from the effective protection of robust oxide glass, lanthanide-doped $CsRe_2F_7$ nanocrystals show long-term stability in harsh environments, retaining near 100% luminescence after directly immersing them in water/oil for 30 days. It is expected that the present nanocomposites have potential applications in the fields of high-end upconversion anti-counterfeiting and high-energy radiation detection.

Received 9th October 2019,
Accepted 4th November 2019

DOI: 10.1039/c9nr08656k

rsc.li/nanoscale

Introduction

Upconversion (UC) or the anti-Stokes process, which is characterized by a two- or multi-photon absorption mechanism to yield shorter-wavelength emission upon longer-wavelength excitation, has been extensively studied for promising applications in bioassay, displays, photovoltaics and lasers.[1,2] Benefitting from their partially filled 4f orbitals, tri-valence lanthanide (Ln^{3+}) ions possess a multitude of meta-stable energy levels with long decay lifetimes, making them ideal activators for UC luminescence.[3–10] Among diverse hosts, fluorides have attracted the most attention for their relatively low phonon energies, which leads to a decrease in the non-radiative de-excitation probability that significantly affects the UC luminescence quantum yield (ULQY).[2] Indeed, Ln-doped UC fluoride nanocrystals (NCs) have been extensively explored as a new category of luminescent labels that have become promising alternatives to the organic fluorophores and quantum dots applied in biological assays and medical imaging, owing to their unique optical performance, such as sharp emission bands, long luminescence lifetimes (micro- to milliseconds), good photostability, low background autofluorescence, and low toxicity.[11–15] So far, fluoride NCs, such as MF_2 (M = Ca, Sr, Ba), ReF_3 (Re = La, Gd, Y, Lu), $AReF_4$ (A = Li, Na, K) and $BaYF_5$ that have high solubility for Ln^{3+} dopants, have been widely adopted as UC hosts.[16–23] Especially, hexagonal β-$NaYF_4$ co-doped with Yb^{3+}/Er^{3+}(Tm^{3+}) is regarded as the most efficient green (blue) UC material.[24–27]

Considering the dispersion relationship in that the lattice vibration frequency is inversely proportional to atomic mass, and cesium (Cs) is the heaviest alkali metal of the first main

[a]College of Physics and Energy, Fujian Normal University, Fujian Provincial Key Laboratory of Quantum Manipulation and New Energy Materials, Fuzhou, 350117, China. E-mail: dqchen@fjnu.edu.cn
[b]Fujian Provincial Collaborative Innovation Center for Optoelectronic Semiconductors and Efficient Devices, Xiamen, 361005, China
[c]Fujian Provincial Engineering Technology Research Center of Solar Energy Conversion and Energy Storage, Fuzhou, 350117, China

†Electronic supplementary information (ESI) available: Tables S1–S4, Fig. S1–S35, ESI movie. Theoretical calculation of laser-irradiation-induced temperature for Er:$CsYb_2F_7$@glass. Extra crystal structure, FTIR, Raman, and XPS spectra, XRD patterns, HRTEM image, HAADF-STEM images, elemental mapping, UC emission spectra, decay curves, CIE diagrams, energy levels and luminescent photographs. See DOI: 10.1039/c9nr08656k

group except for the radioactive element francium (Fr), the lattice vibration frequency (phonon energy) of Cs-containing Re fluorides will be lower than that of Na-based Re ones, and superb UC performance is expected when doping Ln^{3+} emitting centers into them. Additionally, the Cs ion has a strong X-ray absorption coefficient compared to other alkali metals, since X-ray attenuation is proportional to atomic number.[28] Therefore, Cs-based compounds have potential applications as detectors for high-energy ray irradiation. In fact, ternary fluoride compounds of $CsRe_2F_7$ (Re = Y, Gd, Lu) have been quickly adopted as laser and scintillation hosts for multiple Re^{3+} sites (Table S1, Fig. S1†), synthesized by solid-state reactions or fluorination of solid compounds at high temperatures.[29–32] These bulky samples are fabricated under very drastic conditions starting from Re oxides and alkali metal fluorides in aqueous solutions. Recently, Yb/Er-doped CsY_2F_7 UCNCs were prepared in high boiling organic solvent for the first time by Haase *et al.*, but the UC luminescence was reported to be far lower than that of Yb/Er:β-$NaYF_4$.[33] On the other hand, Yb/Er/Tm-doped $CsLu_2F_7$ NCs were synthesized *via* a solvothermal method and employed as the CT/UCL imaging agent for chemo-thermal synergistic therapy.[34] To the best of our knowledge, the general synthesis of a whole family of $CsRe_2F_7$ (Re = La–Lu, Y, Sc) NCs has not been reported and the related optical properties have not been well understood. Notably, Cs-based compounds are usually liable to deliquesce in the air and suffer from poor long-term stability, which will significantly limit their practical applications.

Benefitting from superior thermal, mechanical, and chemical stabilities, oxide glasses with flexibility in composition and amorphous structures have been widely employed as the hosts for various nano-/micro-crystals, including quantum dots, fluoride NCs and oxide phosphors to improve their stability.[35] In particular, several Ln-doped fluoride UCNCs, such as Yb/Er:β-$NaYF_4$, have been successfully embedded in glasses.[36–42] In this method, a critical point is to elaborately design the glass network and appropriately control nucleation/growth (or precipitation) of fluoride NCs from the glass matrix through heating glass above the glass transition temperature.[43] However, the diffusion of Cs ions in glass requires a large activation energy due to its heavy atomic mass, leading to the formidably difficult precipitation of Cs-containing fluorides in glass. As far as we know, there are still no any reports on the growth of Cs-based fluoride NCs in glasses.

In this work, we report the controllable *in situ* crystallization of a whole family of hexagonal cesium rare earth fluorides, β-$CsRe_2F_7$ (Re = La–Lu, Y, Sc), inside aluminosilicate glass (denoted as $CsRe_2F_7$@glass) for the first time. A highest ULQY of 0.67% is achieved for Yb/Er:$CsLu_2F_7$@glass, which is far better than that of the well-known Yb/Er:β-$NaYF_4$ (hexagonal phase) in glass. A remarkable photothermal effect is observed for Er:$CsYb_2F_7$@glass, enabling control of its UC emissive color by pumping laser power and finding practical application in high-end anti-counterfeiting. Besides this, it is demonstrated that Ce:$CsYb_2F_7$@glass can yield highly efficient radioluminescence upon X-ray irradiation. These impressive optical properties of $CsRe_2F_7$@glass products are mainly attributed to low lattice vibrations, reduced loss of non-radiative relaxation and effective protection of the robust glass matrix.

Experimental section

Fabrication of $CsRe_2F_7$@glass samples

The starting materials for the mother glass were SiO_2, Al_2O_3, Cs_2CO_3, CsF and ReF_3. The glass compositions (Table S1†) were elaborately designed to achieve the precipitation of hexagonal β-$CsRe_2F_7$ (Re = La–Lu, Y, Sc) phase in glass *via in situ* crystallization. A series of down-shifting emissive samples was prepared by introducing dopants such as Eu^{3+} and Ce^{3+} from additives of EuF_3 and CeF_3, while the study of UC luminescence was performed by adding ErF_3, HoF_3, and TmF_3. In a typical synthesis, about 15 g of raw materials was mixed adequately and melted in a muffle furnace at 1550 °C for 40 min in air. The melted sample was poured into a pre-heated copper mold (350 °C) quickly to prepare the precursor glass (PG). The synthesized sample was annealed below the glass transition temperature to reduce internal stress. Finally, the PG was heat-treated at 700–950 °C for 2 h to induce fluoride crystallization in the glass matrix to produce the $CsRe_2F_7$@glass product.

Physical characterization

The crystalline phase structures inside the glass were identified by X-ray diffraction (XRD) using a Rigaku MiniFlex II X-ray diffractometer with Cu Kα radiation (λ = 1.542 Å) in the 2θ range from 10° to 70° with a scanning speed of 5° per minute. The infrared vibration spectra in the range of 400–1600 cm^{-1} were recorded using a Nicolet 8700 Fourier-transform infrared spectrophotometer. Raman spectra of PG and $CsLu_2F_7$@glass in the range of 100–1500 cm^{-1} were recorded by a LabRam HR Raman spectrometer operated with 532 nm laser excitation. Since the photoluminescence of Er^{3+} excited by a 532 nm laser can cause background noise, Raman measurements were performed on Er^{3+}-free samples. Microstructural observations on $CsLu_2F_7$@glass were conducted on a JEOL JEM-2010F transmission electron microscope (TEM) at a 200 kV accelerating voltage and an FEI aberration-corrected Titan Cubed S-Twin TEM operated in high-angle annular dark-field mode. The chemical and elemental environments in PG and $CsLu_2F_7$@glass were detected by XPS using a VG Scientific ESCA Lab Mark II spectrometer equipped with two ultra-high vacuum (UHV) chambers and C_{1s} peaks on indeterminate surfaces using 284.6 eV of carbon as a reference. ^{27}Al, ^{19}F and ^{29}Si magic-angle spinning nuclear magnetic resonance (MAS-NMR) spectra were recorded using a Bruker ADVANCE III HD 400 instrument with a spinning rate of 34 kHz.

Optical measurements

Photoluminescence (PL), upconversion (UC) emission spectra and time-resolved spectra were recorded on an Edinburgh Instruments FLS1000 spectrofluorometer equipped with 450 W xenon lamps, 60 W pulse xenon lamps and 980 nm diode laser as the excitation sources. The corresponding decay lifetimes were evaluated by using the equation $\tau = \int I(t)dt/I_0$, where I_0 is the peak intensity and $I(t)$ is the time-related emissive intensity. A Linkam THMS600 temperature controlling stage was used to record temperature dependent UC emission spectra. The laser power density was measured by using an IR Power Meter laser power meter (CNI TS15). Time-resolved PL traces for Ce^{3+} emission in Ce:$CsLu_2F_7$@glass samples were detected on a fluorescent lifetime spectrometer (Edinburgh Instruments, LifeSpec-II) based on a time correlated single photon counting technique under the excitation of 375 nm picosecond laser. The temperature was recorded by a laser sight infrared thermometer (Optris LS) with a temperature resolution of 0.1 °C in the temperature range of −35–900 °C. The temperature data were directly detected from the surfaces of Er:$NaYbF_4$@glass, Er:$KYbF_4$@glass, Er:KYb_2F_7@glass and Er:$CsYb_2F_7$@glass samples. The emissivity coefficient was set to be 0.95. An infrared thermal imager (Fluke Ti10) was employed to characterize the temperature and thermal distribution of the glass samples. UC luminescence quantum yield (ULQY) and PLQY values for the investigated samples were determined by combining an integrated sphere in an FLS1000 spectrofluorometer. The radioluminescence spectra of Ce:$CsLu_2F_7$@glass were recorded using an X-ray excited spectrometer, in which a Au anticathode target was used as the X-ray source operating at 40 kV and 50 μA.

Results and discussion

The appropriate design of glass composition and network structure is an essential prerequisite for the nucleation/growth of $CsRe_2F_7$ NCs in glass (Table S2†). Herein, precursor glass (PG) with a composition of SiO_2–Al_2O_3–Cs_2CO_3–CsF–ReF_3 was prepared by a melt-quenching method. Typical amorphous humps can be observed in the XRD pattern of PG, and distinct diffraction peaks assigned to the hexagonal $CsRe_2F_7$ phase appear after heat-treatment at 700–950 °C for 2 h (Fig. 1a), indicating the successful growth of $CsRe_2F_7$ crystals in glass. XRD peaks shift toward a larger angle when the precipitated phase changes from $CsLa_2F_7$ to $CsLu_2F_7$ due to the lanthanide contraction effect (Table S2†). The calculated lattice parameters (a and c) are determined based on the XRD patterns and Bragg formula (Table S3†), showing a tendency of lattice expansion with a decrease in the Re ionic radius from La (1.19 Å) to Sc (0.89 Å). Notably, the required crystallization temperature is gradually elevated from $CsLa_2F_7$ to $CsLu_2F_7$ owing to the large diffusion activation energy for heavier Re ions (Table S2†). Taking $CsLu_2F_7$@glass as a typical example, the high-angle annular dark-field scanning transmission electron microscopy (HAADF-STEM) micrograph (Fig. 1b) evidences the distribution of $CsLu_2F_7$ NCs with sizes of 30–80 nm inside the glass matrix. The obvious contrast between $CsLu_2F_7$ NCs (bright) and aluminosilicate glass (dark) can be distinctly discerned because of the large difference of atomic number between Cs/Lu (Z = 55/71) and Al/Si (Z = 14/13). Elemental mappings confirm the segregation of Cs, Lu and F in the NCs and the homogeneous distribution of Si and O in the glass matrix (Fig. 1c). The high-resolution TEM image (Fig. S2†) verifies their high-crystallinity with well-resolved lattice fringes. As evidenced in Fig. 1b, all the $CsRe_2F_7$@glass monolithic materials are transparent and show characteristic colors of the corresponding Re compounds.

The FTIR spectra of PG and $CsLu_2F_7$@glass (Fig. S3†) exhibit a bending vibration (447 cm^{-1}), symmetric stretching vibration (776 cm^{-1}) and anti-symmetric stretching vibration (1046 cm^{-1}) of [SiO_4] and [AlO_4] units.[44] An extra 595 cm^{-1} vibration band is attributed to the [AlO_6] octahedron in the glass structure. The Raman spectra (Fig. S4†) show a bending vibration of Si–O–Si (300–500 cm^{-1}), symmetric stretching vibration (600 cm^{-1}) of Al–O_{nb} (O_{nb} represents non-bridging oxygen), symmetrical bending vibration of O–Si–O (790 cm^{-1}) and the anti-symmetric stretching vibration of Si–O_{nb}–Si (1100 cm^{-1}).[45–47] All the results indicate that the present glass network structure is mainly composed of [SiO_4] and [AlO_4] tetrahedrons. ^{27}Al and ^{29}Si magic angle spinning (MAS) nuclear magnetic resonance (NMR) spectra of PG and $CsLu_2F_7$@glass (Fig. 1d and e) evidence that both samples exhibit the same resonance band at 50 and −105 ppm, attributed to [AlO_4] and [SiO_4], respectively,[48,49] which is well consistent with the results of the FTIR and Raman spectra. As for the ^{19}F MAS-NMR spectra, two resonance bands at −190 and −152 ppm are observed for PG and only a broad resonance band in the range of −165 to −119 ppm is detected for $CsLu_2F_7$@glass (Fig. 1f). The F signal at −190 ppm is assigned to F in the glass while that at −152 is located in the spectral region for F in the $CsLu_2F_7$ NCs.[48,50–52] This result indicates that $CsLu_2F_7$ nuclei have already pre-formed in the PG and heat-treatment can promote the release of other F ions from the glass to take part in fluoride crystallization. X-ray photoelectron spectroscopy (XPS) data (Fig. S5†) demonstrate the presence of Cs, F, Al, C, Lu, Si and O signals. The slight shift in the signals of Cs, Lu, and F towards a larger binding energy after crystallization, especially for Lu, is attributed to the alteration of these elemental environments, *i.e.*, the precipitation of $CsLu_2F_7$ NCs from glass.

Taking Eu^{3+} as a structural probe, PL spectra and time-resolved spectra of Eu^{3+}-doped PG and $CsRe_2F_7$@glass (Re = La, Gd, Y, Lu, Yb, Sc) were recorded to trace the local environment variations of dopants after crystallization (Fig. S6–S11†). Eu^{3+} emission bands of PG show a typical inhomogeneous broadening due to its amorphous environment. After $CsRe_2F_7$ crystallization, Eu^{3+} emissive bands undergo Stark-splitting, decay lifetimes are elongated and emissions producing from higher $^5D_{1,2}$ excited states are enhanced. Additionally, compared to PG, the integrated intensity ratio between the electric dipolar $^5D_0 \rightarrow {}^7F_2$ transition and magnetic dipolar $^5D_0 \rightarrow {}^7F_1$ one for Eu:$CsRe_2F_7$@glass obviously decreases (Fig. S12†). It was concluded that Eu^{3+} dopants partition into a $CsRe_2F_7$ crystalline lattice by substituting Re host ions rather than staying in the glass matrix. This result is reasonable since the whole family of $CsRe_2F_7$ crystalline phases can be precipitated from

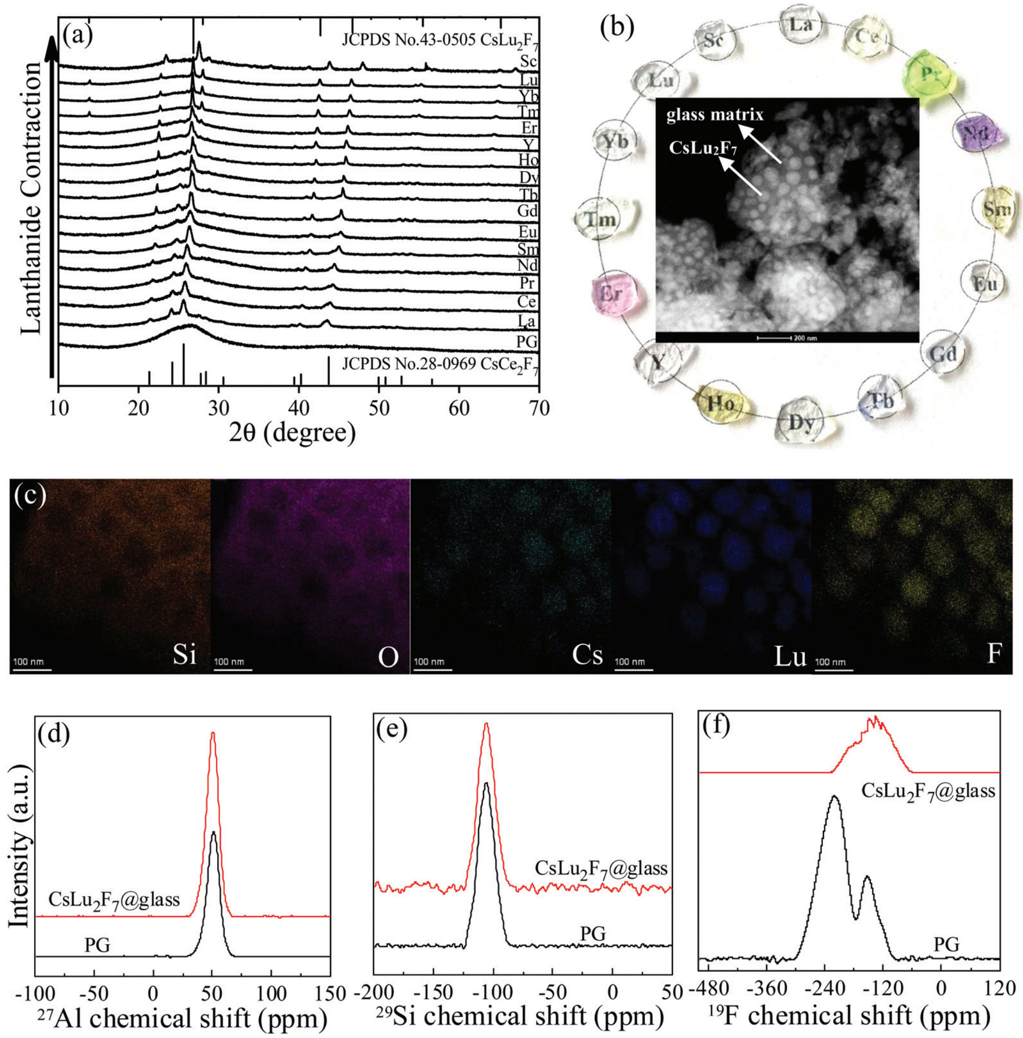

Fig. 1 (a) XRD patterns of β-$CsRe_2F_7$@glass samples (Ln = La–Lu, Y, Sc). Bars represent standard hexagonal $CsLu_2F_7$ (JCPDS no. 43-0505) and $CsCe_2F_7$ (JCPDS no. 28-0969) crystal data. (b) Photographs of β-$CsRe_2F_7$@glass monolithic materials and a typical HAADF-STEM image of β-$CsLu_2F_7$@glass. (c) Si, O, Cs, Lu and F elemental mapping of the $CsRe_2F_7$@glass sample. (d) ^{27}Al, (e) ^{29}Si and (f) ^{19}F MAS-NMR spectra for PG and β-$CsLu_2F_7$@glass.

glass in the present system and Ln^{3+} dopants easily incorporate into the $CsRe_2F_7$ lattice to form a solid-solution *via* heat treatment.

Taking Yb/Ln (Ln = Er, Ho, Tm) doped $CsLu_2F_7$@glass as a typical example, the UC emission spectra show characteristic Er^{3+} green ($^2H_{11/2}$,$^4S_{3/2}$ → $^4I_{15/2}$) and red ($^4F_{9/2}$ → $^4I_{15/2}$), Ho^{3+} green ($^5S_2$,$^5F_4$ → $^5I_8$) and red ($^5F_5$ → $^5I_8$), and Tm^{3+} blue ($^1G_4$ → $^3H_6$, $^1D_2$ → $^3F_4$) and red ($^5F_{2,3}$ → $^3H_6$) transitions, respectively, yielding yellow, green and blue UC luminescent colors (Fig. 2a). Notably, the UC intensities of Yb/Ln:$CsRe_2F_7$@glass samples are about 3–40 times higher than those of the corresponding PGs (Fig. S13–S19†) and obvious elongated UC decay lifetimes are observed (Fig. S20†). These results are attributed to the alteration of Ln^{3+} ligand-fields after glass crystallization, *i.e.*, a partition from amorphous glass with a high phonon energy into the $CsRe_2F_7$ crystalline lattice with a low phonon energy. Fig. 2b shows the host-dependent UC emission behaviors for the Yb/Er:$CsRe_2F_7$@glass (Re = La, Y, Gd, Yb, Lu, Sc) samples. All the products exhibit characteristic Er^{3+} green and red emissions but produce remarkably distinct red-to-green (R/G) UC emissive ratios for different fluoride crystalline environments (Fig. S21†). A rapid rise in the R/G ratios for Yb/Er doped $CsLa_2F_7$, $CsGd_2F_7$, CsY_2F_7, $CsLu_2F_7$ and $CsSc_2F_7$ is attributed to the difference in the ionic radii of La^{3+} (1.19 Å), Gd^{3+} (1.08 Å), Y^{3+} (1.04 Å), Lu^{3+} (1.00 Å) and Sc^{3+} (0.89 Å), which results in gradually shortened La–La, Gd–Gd, Y–Y, Lu–Lu and Sc–Sc distances in hexagonal $CsRe_2F_7$ fluoride lattices. Consequently, Er^{3+} and Yb^{3+} dopants in the $CsRe_2F_7$ lattice by substituting Re^{3+} ions create closer Yb–Er cation pairs in the order of $CsLa_2F_7$ > $CsGd_2F_7$ > CsY_2F_7 > $CsLu_2F_7$ > $CsSc_2F_7$, leading to a gradual increase in R/G ratio and a change of UC color from green to yellow (insets of Fig. S21†). The highest R/G ratio and red UC emissive color for the Er:$CsYb_2F_7$@glass

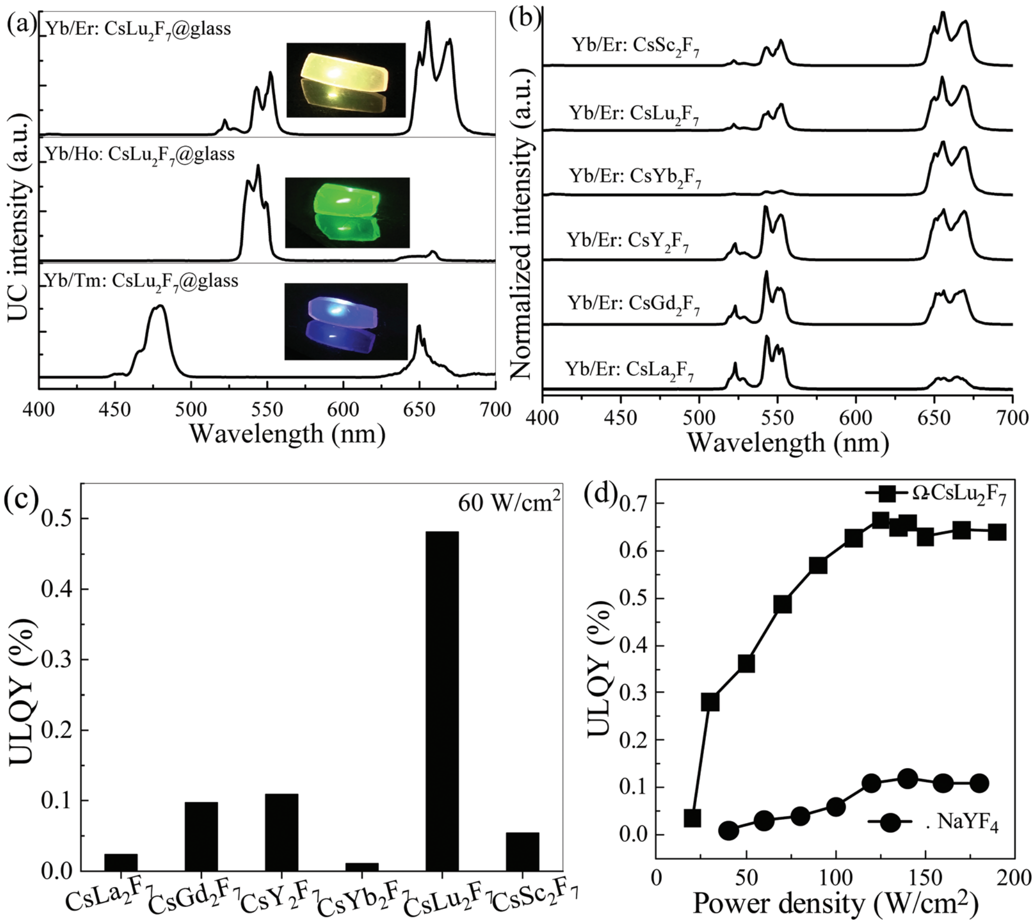

Fig. 2 (a) UC emission spectra of Yb/Er, Yb/Ho, and Yb/Tm doped $CsLu_2F_7$@glass samples. Insets are the corresponding UC emissive photographs under the irradiation of 980 nm laser. (b) UC emission spectra of Yb/Er:$CsRe_2F_7$@glass (Re = La, Gd, Y, Yb, Lu, Sc) samples. (c) ULQY values of Yb/Er:$CsRe_2F_7$@glass upon exposure to a laser power density of 60 W cm^{-2}. (d) Comparison of ULQYs between Yb/Er:$CsLu_2F_7$@glass and Yb/Er:β-$NaYF_4$@glass pumped with various power densities.

(Fig. S21†) are due to the high-content (100%) Yb^{3+} ions in the $CsYb_2F_7$ crystal host, which promotes Yb-to-Er energy transfer to efficiently populate the Er^{3+} $^4F_{9/2}$ red-emitting state.

To compare UC performance, absolute ULQY values were determined with the aid of an integrating sphere and a near-infrared (NIR, 200–1010 nm) PMT detector. The ULQYs for glass-stabilized Yb/Er doped $CsLa_2F_7$, CsY_2F_7, $CsGd_2F_7$, $CsYb_2F_7$, $CsLu_2F_7$ and $CsSc_2F_7$ under the pumping power density of 60 W cm^{-2} are 0.024%, 0.097%, 0.109%, 0.011%, 0.481% and 0.054%, respectively (Fig. 2c). Among these different hosts, the highest ULQY for Yb/Er:$CsLu_2F_7$@glass is ascribed to the heaviest Lu atom in the host, which induces the lowest lattice vibration with low Er^{3+} non-radiative loss, while the lowest ULQY for Er:$CsYb_2F_7$@glass is due to the concentration quenching effect of 100% Yb^{3+} host ions. Furthermore, power density dependent ULQYs for Yb/Er:β-$CsLu_2F_7$@glass and Yb/Er:β-$NaYF_4$@glass were obtained and are compared in Fig. 2d. Yb/Er:β-$NaYF_4$@glass was prepared *via* the elaborate design of glass composition and a similar glass crystallization strategy, and the particle sizes (40–100 nm) of β-$NaYF_4$ inside the glass were tuned to be close to those of β-$CsLu_2F_7$ ones to enable the comparison of UC performance (Fig. S22, Table S2†). Evidently, the ULQY of Yb/Er:$CsLu_2F_7$@glass (0.67%) is about 6 times higher than that of Yb/Er:$NaYF_4$@glass (0.11%) at a high powder density (125–180 W cm^{-2}), which is ascribed to the heavier Cs and Lu in the former host than Na and Y in the latter one. The ULQY values for the Yb/Ho:$CsLu_2F_7$@glass and Yb/Tm:$CsLu_2F_7$@glass (400–700 nm) samples are 0.16% and 0.04% under a laser power density of 60 W cm^{-2}, respectively. As evidenced in Fig. S23,† UC emission intensities of Yb/Er-, Yb/Tm-, and Yb/Ho-doped $CsLu_2F_7$@glass products are about 3, 13, and 5 times higher than those of $NaYF_4$@glass ones, verifying that the UC performance of Yb/Ln-doped hexagonal $CsLu_2F_7$ is indeed better than that of the corresponding hexagonal $NaYF_4$.

Interestingly, it was found that Er:$CsYb_2F_7$@glass exhibits obvious 980 nm laser-power-dependent UC luminescence (Fig. S24a†), *i.e.*, a remarkable photothermal effect. With an increase in the laser power, the UC emission color gradually alters from red to green (Fig. S24b†) and the color variation is recyclable without inducing any changes in the crystalline phase structure (see Movie S1 and Fig. S25†). The corres-

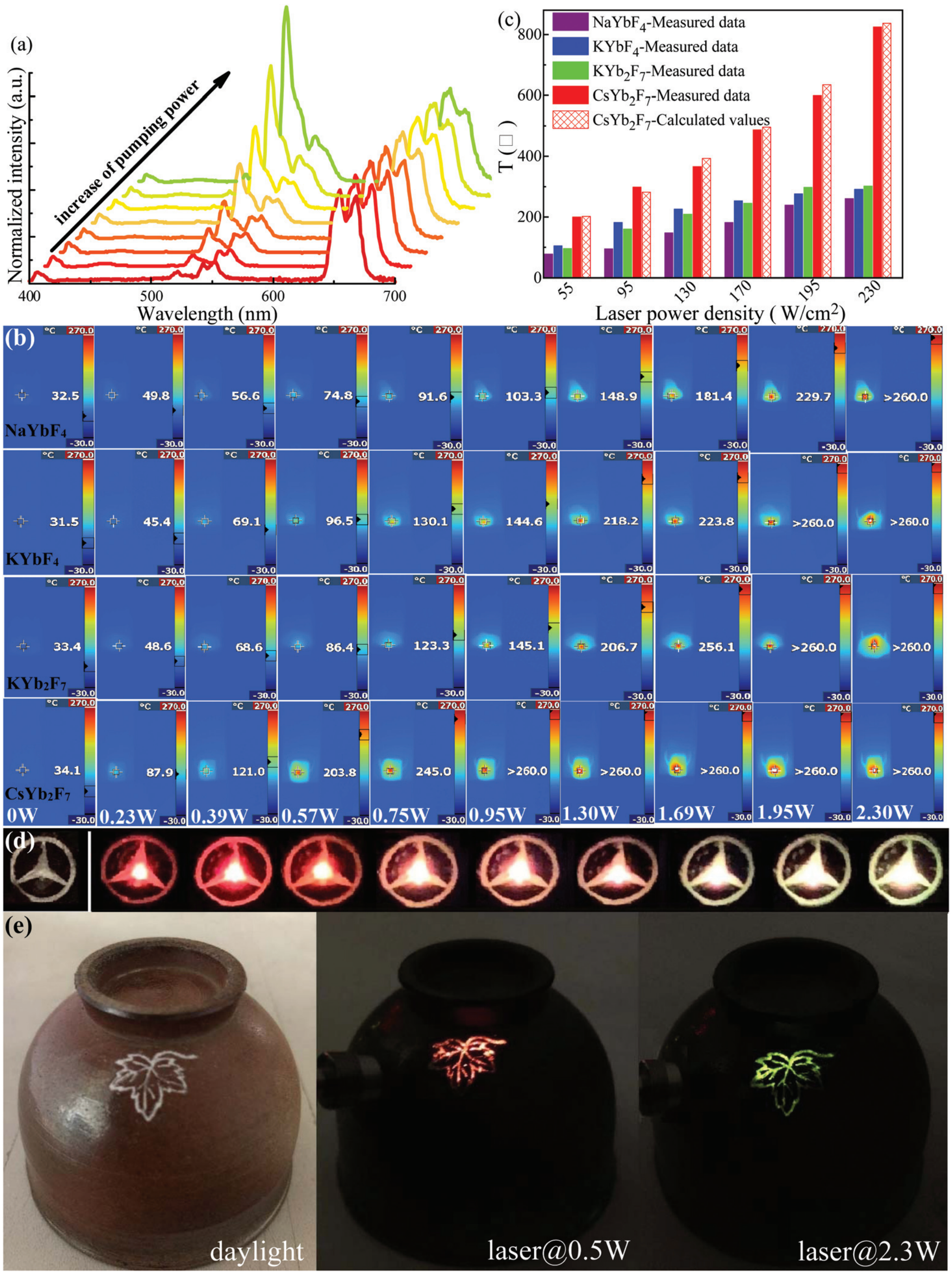

Fig. 3 (a) Laser power dependent UC emission spectra of Er:$CsYb_2F_7$@glass (all the spectra are normalized to the Er^{3+} red emission band). (b) Infrared thermal images recorded from Er:$NaYbF_4$@glass (first row), Er:$KYbF_4$@glass (second row), Er:KYb_2F_7@glass (third row) and Er:$CsYb_2F_7$@glass (fourth row) samples under irradiation of 980 nm laser (laser power gradually increases from left to right: 0, 0.23, 0.39, 0.57, 0.75, 0.95, 1.30, 1.69, 1.95 and 2.30 W). The detected temperatures are presented in each figure. (c) The experimental measured and theoretical calculated temperatures for the corresponding samples exposed to different 980 nm laser power densities. (d) Variable UC emissive colors for the designed Mercedes–Benz pattern using Er:$CsYb_2F_7$@glass under laser irradiation (laser power increases from left to right). (e) Anti-counterfeiting demonstration of Chinese Dehua porcelain decorated by an Er:$CsYb_2F_7$@glass flower pattern.

ponding UC spectra (Fig. S24a,† Fig. 3a) evidence that the color variation originates from the significant enhancement of the green emission band assigned to the Er^{3+} $^2H_{11/2} \rightarrow {}^4I_{15/2}$ transition. This result indicates that the variation of emissive color is due to the significantly increased electron population in the Er^{3+} $^2H_{11/2}$ excited state *via* laser-induced thermal activation from the thermally coupled Er^{3+} $^4S_{3/2}$ state (Fig. S26a†). Notably, it was found that the population of the $^4S_{3/2}$ excited state related to that of the $^4F_{9/2}$ one is remarkably enhanced with an increase of laser pumping power (Fig. S26b–S26d†), which is beneficial to populating the thermal-coupled $^2H_{11/2}$ state from the $^4S_{3/2}$ one by raising laser power. Additionally, the same sample under liquid nitrogen cooling (at 77 K) shows no significant increase in the Er^{3+} $^2H_{11/2} \rightarrow {}^4I_{15/2}$ UC emission relative to that of Er^{3+} $^4S_{3/2} \rightarrow {}^4I_{15/2}$ (Fig. S27†), confirming that the enhanced population of the Er^{3+} $^2H_{11/2}$ state is indeed induced by an incident 980 nm laser thermal effect. As a comparison, Er:$NaYbF_4$@glass, Er:$KYbF_4$@glass, and Er:KYb_2F_7@glass were prepared (Fig. S28, Table S2†); however, their UC emission spectra exhibit only a certain degree of enhanced green Er^{3+} $^2H_{11/2} \rightarrow {}^4I_{15/2}$ emission with an elevation in the laser power (Fig. S29†). For all four samples, the incident 980 nm laser can be efficiently absorbed by 100% Yb^{3+} ions in the hosts; however, compared to the other samples, the energy is not easily dissipated in the Er:$CsYb_2F_7$@glass sample due to the lowest lattice vibration of the host with heavy Cs ions. Therefore, this unique laser-induced UC color change is attributed to the high Yb content (100%) and low lattice vibration for heavier Cs than K/Na in the fluoride hosts.

To quantitatively and visually characterize the laser-induced temperature change in these samples, real-time infrared thermal images with 980 nm laser irradiation (0–2.30 W) on the four kinds of NC embedded glasses were recorded (Fig. 3b). They clearly illustrate that the temperature gradually rises with an increase in the laser power for all the samples, but the elevating speed of the temperature in the Er:$CsYb_2F_7$@glass sample is much faster than that in the other three samples. The comparison of temperature variation in these four samples recorded using a laser sight infrared thermometer is provided in Fig. 3c and Fig. S30.† The temperature in the Er:$CsYb_2F_7$@glass sample can reach as high as 800 °C upon 230 W cm^{-2} laser irradiation, while the temperatures in the other three samples only reach about 300 °C. Theoretical calculated laser-induced temperatures of Er:$CsYb_2F_7$@glass based on the fluorescence intensity ratio between $^2H_{11/2}$ and $^4S_{3/2}$ thermally coupled states (Fig. S31 and Table S4†)[53] are also provided in Fig. 3c, and they are coincident with the measured values.

The remarkable laser-induced photothermal effect for the Er:$CsYb_2F_7$@glass sample enables it to have novel anti-counterfeiting application potential. As demonstrated in Fig. 3d, a Mercedes–Benz pattern was designed using Er:$CsYb_2F_7$@glass, which shows obvious variation in the UC emissive color with an increase in the incident 980 nm laser power. Further, Chinese Dehua porcelain decorated by Er:$CsYb_2F_7$@glass can produce a red UC flower pattern when exposed to 0.5 W laser,

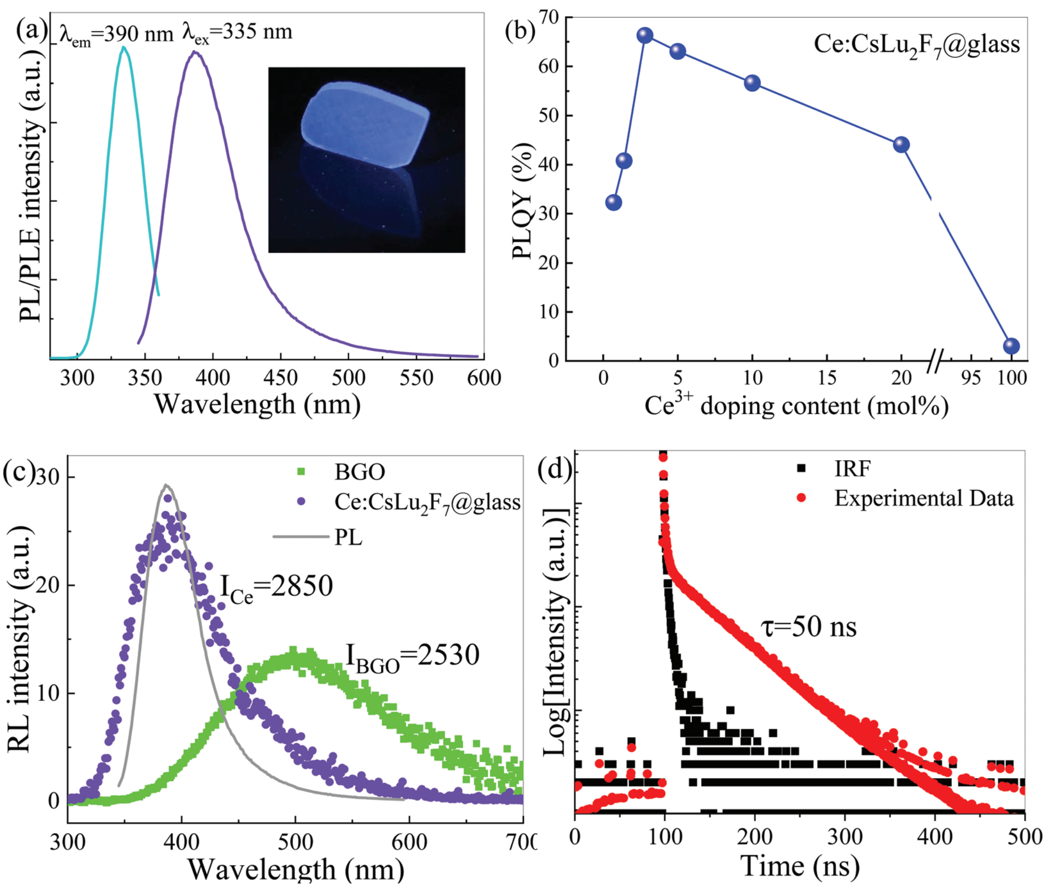

Fig. 4 (a) PLE and PL spectra of Ce:$CsLu_2F_7$@glass. Inset is the luminescence photograph of the Ce:$CsLu_2F_7$@glass monolith under the irradiation of a UV lamp. (b) Ce-Content-dependent PLQY values of Ce:$CsLu_2F_7$@glass. (c) RL spectrum of Ce:$CsLu_2F_7$@glass upon the irradiation of X-ray. The corresponding PL spectrum of Ce:$CsLu_2F_7$@glass and RL spectrum of standard BGO crystal are provided. (d) Time-resolved emission spectrum of Ce:$CsLu_2F_7$@glass. IRF represents instrumental response function.

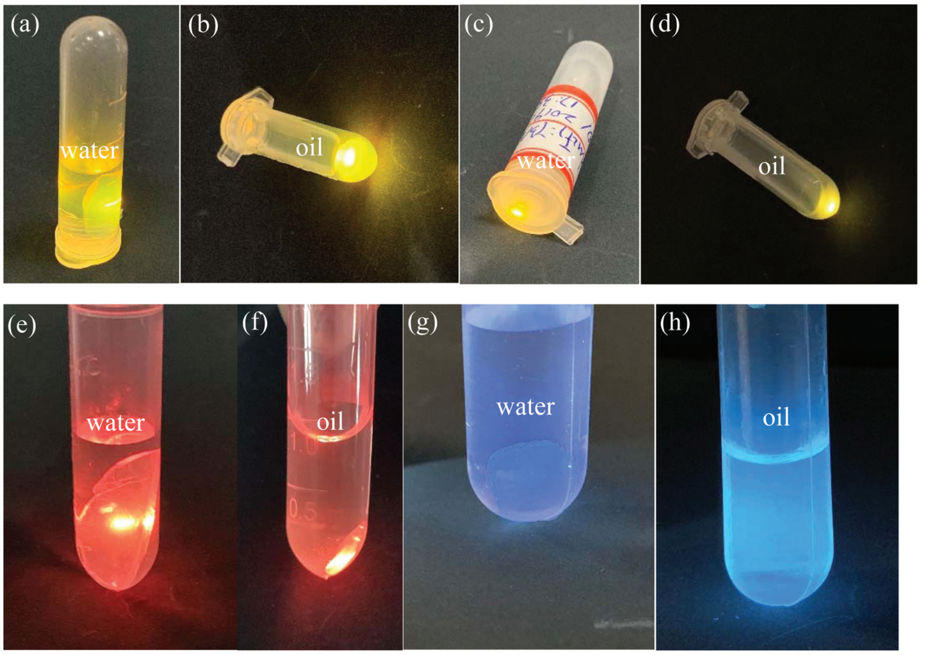

Fig. 5 UC emissive photographs of (a and b) Yb/Er:$CsLu_2F_7$@glass monolith, (c and d) Yb/Er:$CsLu_2F_7$@glass powders and (e and f) Er:$CsYb_2F_7$@glass (λ_{ex} = 980 nm) after immersing in water and oil solutions for 90 days. (g and h) Luminescence photographs of Ce:$CsLu_2F_7$@glass (λ_{ex} = 365 nm) after immersing in water and oil solutions for 90 days.

and the flower changes to green after laser power increases up to 2.3 W (Fig. 3d). Moreover, it is also feasible to modify the UC luminescent color upon fixed laser irradiation (0.5 W) by directly changing the sample temperature *via* heating (Fig. S32†).

Furthermore, we demonstrate the possible application of a Ce-doped $CsLu_2F_7$@glass monolith as a scintillator material. PL and PL excitation (PLE) spectra show typical broad absorption and emission bands of the allowed Ce^{3+} 4f ↔ 5d transitions (Fig. 4a). Compared to the absorption band (~335 nm), a Stokes shift (~55 nm) is observed for the 5d → 4f emission (~390 nm), ascribed to the vibration relaxation of the $CsLu_2F_7$ host. The Ce:$CsLu_2F_7$@glass monolith with dimensions of 5 cm × 5 cm can be easily fabricated (inset of Fig. 4a). With an increase in the Ce^{3+} doping content, a slight red-shift in the PL band is observed owing to the re-absorption effect (Fig. S33a†). PLQY values obtained for a series of Ce^{3+}-doped samples indicate that the optimal Ce^{3+} doping content is 2.8 mol% and the highest PLQY reaches as high as 67% (Fig. 4b). Remarkably, under X-ray beam irradiation, the Ce:$CsLu_2F_7$@glass yields intense broadband radioluminescence (RL) with a peak wavelength of ~390 nm (Fig. 4c), coinciding with the PL spectrum. Notably, compared to the PL band, the RL band shows a certain degree of broadening. By contrast, the RL spectrum of conventional bulk $Bi_4Ge_3O_{12}$ (BGO, Kinheng Crystal, China.) scintillators is also provided and the RL intensity of Ce:$CsLu_2F_7$@glass is about 115% that of BGO (Fig. 4c). Upon pulse light excitation, time-resolved spectra of Ce:$CsLu_2F_7$@glass samples were recorded by monitoring Ce^{3+} emission (Fig. S33b†), which shows a nearly single-exponential decay behavior with a fitted lifetime of ~50 ns for the 2.8 mol% Ce-doped $CsLu_2F_7$@glass sample (Fig. 4d). This fast response to X-ray irradiation is critical to scintillation performance in medical radiography. All these results verify the potential application of the present product as a novel scintillator.

Finally, the stability of Yb/Er:$CsLu_2F_7$@glass was studied by directly immersing it in aqueous or oil solutions for different durations. The UC spectra show that there is no obvious change in the spectral intensity and profile (Fig. S34a and S34b†) and near 100% intensity can be retained after immersing the product (as a glass monolith or in powder form) in aqueous solution for 30 days (Fig. S34c and S34d†). UC decay curves obtained by monitoring Er^{3+} green and red emissions verify that the radiative kinetics of Er^{3+}:$^4S_{3/2}$ and $^4F_{9/2}$ states are not remarkably affected by increasing the storage time in water/oil (Fig. S35†). As evidenced in Fig. 5, intense UC luminescence for the Yb/Er:$CsLu_2F_7$@glass and Er:$CsYb_2F_7$@glass and bright PL for the Ce:$CsLu_2F_7$@glass remain after immersing them in water or oil for a long period (3 months). Therefore, it can be concluded that the present glass-stabilized $CsRe_2F_7$ NCs with multi-functional emissive features exhibit superior long-term stability, enabling them to find practical applications in the optoelectronic field.

Conclusion

In summary, an *in situ* glass crystallization strategy was developed to realize nucleation/growth of a whole family of hexagonal $CsRe_2F_7$ (Re = La–Lu, Y, Sc) NCs inside aluminosilicate glass for the first time. A maximal ULQY of 0.67% was achieved for Yb/Er:$CsLu_2F_7$ NCs, being far higher than that of the well-known Yb/Er:β-$NaYF_4$ NCs (0.11%). A remarkable photothermal effect was observed for Er:$CsYb_2F_7$ NCs, and the temperature of the sample upon exposure to high-power laser irradiation can reach up to 1000 K. An obvious change of UC emissive color of Er:$CsYb_2F_7$@glass induced by increased laser power enables it to find application in advanced anti-counterfeiting. Besides this, a Ce-doped $CsLu_2F_7$@glass monolith was demonstrated to produce intense violet radioluminescence when exposed to X-ray irradiation and undergo fast radiative decay in the nanosecond scale, showing its potential application as a novel type of scintillator material. Finally, a series of tests proved that the present lanthanide-doped $CsRe_2F_7$ luminescent NCs have superior physicochemical stability owing to the effective protection of the oxide glass. This work provides a new way to fabricate cesium rear-earth fluoride NCs and presents an important advance in exploring innovative high-performance luminescent nanomaterials.

Conflicts of interest

The authors declare no competing financial interests.

Acknowledgements

This research was supported by the National Natural Science Foundation of China (51572065 and 51972060).

References

1 F. Auzel, *Chem. Rev.*, 2004, **104**, 139–172.
2 F. Wang and X. G. Liu, *Chem. Soc. Rev.*, 2009, **38**, 976–989.
3 X. Y. Huang, S. Y. Han, W. Huang and X. G. Liu, *Chem. Soc. Rev.*, 2013, **42**, 173–201.
4 H. Dong, L. D. Sun and C. H. Yan, *Chem. Soc. Rev.*, 2015, **44**, 1608–1634.
5 B. Zhou, B. Y. Shi, D. Y. Jin and X. G. Liu, *Nat. Nanotechnol.*, 2015, **10**, 924–936.
6 X. Zhu, Q. Su, W. Feng and F. Y. Li, *Chem. Soc. Rev.*, 2017, **46**, 1025–1039.
7 D. Hudry, I. A. Howar, R. Popescu, D. Gerthsen and B. S. Richards, *Adv. Mater.*, 2019, **31**, 1900623.
8 D. M. Yang, P. A. Ma, Z. Y. Hou, Z. Y. Cheng, C. X. Li and J. Lin, *Chem. Soc. Rev.*, 2015, **44**, 1416–1448.
9 X. W. Cheng, Y. Pan, Z. Yuan, X. W. Wang, W. H. Su, L. S. Yi, X. J. Xie and L. Huang, *Adv. Funct. Mater.*, 2018, **28**, 1800208.
10 Y. S. Liu, D. T. Tu, H. M. Zhu, R. F. Li, W. Q. Luo and X. Y. Chen, *Adv. Mater.*, 2010, **22**, 3266–3271.
11 S. Fischer, N. D. Bronstein, J. K. Swabeck, E. M. Chan and A. P. Alivisatos, *Nano Lett.*, 2016, **16**, 7241–7247.
12 J. J. Zhou, G. X. Chen, E. Wu, G. Bi, B. T. Wu, Y. Teng, S. F. Zhou and J. R. Qiu, *Nano Lett.*, 2013, **13**, 2241–2246.
13 J. T. Xu, P. P. Yang, M. D. Sun, H. T. Bi, B. Liu, D. Yang, S. L. Gai, F. He and J. Lin, *ACS Nano*, 2017, **11**, 4133–4144.
14 C. Homann, L. Krukewit, F. Frenzel, B. Grauel, C. Wurth, U. Resch-Genger and M. Haase, *Angew. Chem., Int. Ed.*, 2018, **57**, 8765–8769.
15 B. Zhou, L. Yan, L. L. Tao, N. Song, M. Wu, T. Wang and Q. Y. Zhang, *Adv. Sci.*, 2018, **5**, 1700667.
16 G. F. Wang, Q. Peng and Y. D. Li, *J. Am. Chem. Soc.*, 2009, **131**, 14200.
17 D. Q. Chen, Y. L. Yu, F. Huang, P. Huang, A. P. Yang and Y. S. Wang, *J. Am. Chem. Soc.*, 2010, **132**, 9976.
18 G. S. Yi and G. M. Chow, *J. Mater. Chem.*, 2005, **15**, 4460–4464.
19 Q. Liu, Y. Sun, T. S. Yang, W. Feng, C. G. Li and F. Y. Li, *J. Am. Chem. Soc.*, 2011, **133**, 17122–17125.
20 G. Y. Chen, T. Y. Ohulchanskyy, A. Kachynski, H. Agren and P. N. Prasad, *ACS Nano*, 2011, **5**, 4981–4986.
21 G. Y. Chen, T. Y. Ohulchanskyy, R. Kumar, H. Agren and P. N. Prasad, *ACS Nano*, 2010, **4**, 3163–3168.
22 F. Wang and X. G. Liu, *J. Am. Chem. Soc.*, 2008, **130**, 5642–5643.
23 F. Vetrone, V. Mahalingam and J. A. Capbianco, *Chem. Mater.*, 2009, **21**, 1847–1851.
24 A. Aebischer, M. Hostettler, J. Hauser, K. Krämer, T. Weber, H. U. Güdel and H. B. Bürgi, *Angew. Chem., Int. Ed.*, 2006, **45**, 2802–2806.
25 K. Krämer, D. Biner, G. Frei, H. U. Güdel, M. P. Hehlen and S. R. Lüthi, *Chem. Mater.*, 2004, **16**, 1244–1251.
26 J. F. Suyver, J. Grimm, K. W. Krämer and H. U. Güdel, *J. Lumin.*, 2005, **114**, 53–59.
27 J. F. Suyver, J. Grimm, M. K. van Veen, D. Binder, K. W. Krämer and H. U. Güdel, *J. Lumin.*, 2006, **117**, 1–12.
28 D. R. Schaart, P. Dorenbos, C. W. E. van Eijk, R. Visser, C. Pedrini, B. Moine and N. M. Khaidukov, *J. Phys.: Condens. Matter*, 1995, **7**, 3063–3088.
29 A. A. Kaminskii, N. M. Khaidukov, W. Koechner and H. R. Verdun, *Phys. Status Solidi A*, 1992, **132**, K105–K108.
30 C. L. M. de Barros, R. B. Barthem and N. M. Khaidukov, *J. Lumin.*, 1999, **82**, 307–314.
31 V. N. Makhov, N. M. Khaidukov, D. Lo, M. Kirm and G. Zimmerer, *J. Lumin.*, 2003, **102–103**, 638–643.
32 M. Karbowiak, A. Mech and W. Ryba-Romanowski, *J. Lumin.*, 2005, **114**, 65–70.
33 H. Schäfer, P. Ptacek, H. Eickmeier and M. Haase, *J. Nanomater.*, 2009, 685624.
34 Y. X. Liu, L. Y. Li, Q. W. Guo, L. Wang, D. D. Liu, Z. W. Wei and J. Zhou, *Theranostics*, 2016, **6**, 1491–1505.
35 X. F. Liu, J. J. Zhou, S. F. Zhou, Y. Z. Yue and J. R. Qiu, *Prog. Mater. Sci.*, 2018, **97**, 38–96.
36 X. Y. Li, D. Q. Chen, F. Huang, G. C. Chang, J. J. Zhao, X. S. Qiao, X. H. Xu, J. C. Du and M. Yin, *Laser Photonics Rev.*, 2018, **12**, 1800030.
37 X. H. Xu, W. F. Zhang, D. Yang, W. Lu, J. B. Qi and S. F. Yu, *Adv. Mater.*, 2016, **28**, 8045–8050.
38 A. Herrmann, M. Tylkowski, C. Bocker and C. Rüssel, *Chem. Mater.*, 2013, **25**, 2878–2884.
39 C. G. Lin, C. Bocker and C. Rüssel, *Nano Lett.*, 2015, **15**, 6764–6769.

40 S. F. Zhou, N. Jiang, K. Miura, S. Tanabe, M. Shimizu, M. Sakakura, Y. Shimotsuma, M. Nishi, J. R. Qiu and K. Hirao, *J. Am. Chem. Soc.*, 2010, **132**, 17945–17952.
41 Z. G. Gao, S. Guo, X. S. Lu, J. Orava, T. Wagner, L. R. Zheng, Y. Y. Liu, S. Y. Sun, P. P. Yang, J. Ren and Y. Yang, *Adv. Opt. Mater.*, 2018, **6**, 1701407.
42 D. Q. Chen, Y. Z. Peng, X. Y. Li, J. S. Zhong, H. Huang and J. K. Chen, *ACS Appl. Mater. Interfaces*, 2019, **11**, 30053–30064.
43 P. P. Fedorov, A. A. Luginina and A. I. Popov, *J. Fluorine Chem.*, 2015, **172**, 22–50.
44 A. Goel, D. U. Tulyaganov, V. V. Kharton, A. A. Yaremchenko, S. Erilsson and J. M. F. Ferreira, *J. Power Sources*, 2009, **189**, 1032–1043.
45 P. McMillan and B. Piriou, *J. Non-Cryst. Solids*, 1983, **55**, 221–242.
46 T. Rouxel and J. L. Besson, *J. Non-Cryst. Solids*, 1990, **122**, 298–304.
47 E. Dolekcekic, M. J. Pomeroy and S. Hampshire, *J. Eur. Ceram. Soc.*, 2007, **27**, 893–898.
48 R. E. Youngman and M. J. Dejneka, *J. Am. Ceram. Soc.*, 2002, **85**, 1077–1082.
49 R. Youngman, *Materials*, 2018, **11**, 476.
50 F. Munoz, A. de Pablos-Martin, N. Hemono, M. J. Pascual, A. Duran, L. Delevoye and L. Montagne, *J. Non-Cryst. Solids*, 2011, **357**, 1463–1468.
51 M. Sroda and Z. Olejniczak, *J. Mol. Struct.*, 2011, **1001**, 78–82.
52 M. Sroda and Z. Olejniczak, *J. Non-Cryst. Solids*, 2011, **357**, 1696–1700.
53 J. S. Zhong, D. Q. Chen, Y. Z. Peng, Y. D. Lu, X. Chen, X. Y. Li and Z. G. Ji, *J. Alloys Compd.*, 2018, **763**, 34–48.

